
¹ **Wind veer and speed in turbulent Ekman flow part I:
scaling analysis and universal profile model**

³ **Cedrick Ansorge¹ and Hauke Wurps^{2,3}**

⁴
⁵ Submitted March 12, 2025

⁶ **Abstract**

⁷ The profiles of wind speed and direction in turbulent Ekman flow are formulated
⁸ based on asymptotic theory and data from direct numerical simulation. The profile
⁹ of the streamwise component follows the classical viscous, logarithmic and wake
¹⁰ scaling. In the outer layer, the velocity component profiles can be described by an
¹¹ Ekman-spiral with adapted boundary conditions that result in a reduction of the
¹² spiral-like rotation. The span-wise component poses a conceptual challenge to the
¹³ channel-flow analogy in the context of asymptotic matching; it exhibits a mixed
¹⁴ scaling in the surface layer, but follows outer scaling for most of the outer layer.
¹⁵ Viscous stress scales universally across the boundary layer in inner units while
¹⁶ the total stress becomes universal as a function of outer height. This implies a
¹⁷ mixed scaling for the turbulent stress and eddy viscosity across the inner layer and
¹⁸ convergence to a universal scaling as function of the outer height across the outer
¹⁹ layer for increasing scale separation vide Reynolds numbers. The extrapolation to
²⁰ these scaling to atmospheric scale separation is confirmed via large-eddy simulation
²¹ in part II of this manuscript.

²² **Keywords** Direct Numerical Simulation · Scale Separation · Ekman Layer · Surface
²³ Layer · Hodograph

²⁴ **1 Introduction**

²⁵ The Coriolis force bends the apparent path of motion on a rotating sphere and
²⁶ establishes geostrophic equilibrium when in balance with a pressure gradient force.
²⁷ Wind veer away from the wind direction in geostrophic equilibrium is (i) due to
²⁸ direct frictional effects in the very vicinity of the surface and (ii) due to turbulence
²⁹ which exerts indirect frictional effects; these effects cause a slow-down of the mean

¹ FU Berlin, Institut für Meteorologie, Carl-Heinrich-Becker-Weg 6–10, 12165 Berlin, Germany
cedrick@posteo.de

² Carl von Ossietzky Universität Oldenburg, School of Mathematics and Science, Institute of Physics

³ ForWind - Center for Wind Energy Research, Küppersweg 70, 26129 Oldenburg, Germany

wind reducing the Coriolis force thus turning the wind in favor of the pressure gradient force. Not only does the veering set the frame of reference for surface layer theory, it also has effects at small and large scales from large-scale dispersion via plume spreading to cyclone spin-down (Svensson and Holtslag 2009) and on the capabilities of data assimilation and accuracy of surface flux estimates (Brown et al. 2005). From a large-scale perspective, the veering of wind across the planetary boundary layer determines the amount of cross-isobaric mass-flux, commonly referred to as 'Ekman pumping' (Ekman 1905), and it is thus a key factor in the life-cycle of large-scale synoptic systems. Within the atmospheric boundary layer (ABL), directional shear of the wind in the upper part of the surface layer may cause a systematic yaw for tall wind power generation devices where blades reach into the Ekman layer, i.e. that part of the boundary layer where the wind starts to turn; an exact estimate of such effects is critical in the site assessments for wind farms (Calaf et al. 2010; Mirocha et al. 2018).

In the planetary boundary layer, wind veer is characterized by the surface veering angle α defined as the angle between the negative surface shear stress τ_{sfc} and the geostrophic wind. Surface veering α and geostrophic drag $Z \equiv u_*/G$, where the friction velocity $u_* \equiv \sqrt{|\tau_{\text{sfc}}|/\rho}$, uniquely determine the surface drag τ_{sfc} in a turbulent Ekman flow. In any quantitative description of the surface layer, the friction velocity u_* is the dynamic scale and α defines the horizontal alignment of the frame of reference, i.e. the rotation of the surface friction with respect to the outer wind direction. Knowledge about u_* and α is thus a prerequisite for any quantitative theory of the surface layer, and Rossby and Montgomery (1935) constrained the two parameters based on integral relations in the ABL. Asymptotic similarity theory was later used by Tennekes (1973); Blackadar and Tennekes (1968), and–based on his seminal direct numerical simulations (DNS) of Ekman flow–, Spalart (1989) suggested a modification to take into account effects of low to intermediate Reynolds numbers. Later on, constants were re-evaluated with a focus on the ABL based on observations (Högström 1988, 1996) and numerical modelling (Spalart et al. 2008, 2009; Ansorge and Mellado 2014; Ansorge 2019).

Attempts were also undertaken to obtain profiles of the wind speed: One approach is to match the inner and outer layer at a reference height as suggested by Etling (2002); Emeis (2018) (Sec. 21.10; Eq. 21.48); they choose the Prandtl-layer height z_{Prandtl} to match the wind speed profiles, which, however, requires external prescription of $\alpha(z_{\text{prandtl}})$, the veering at that height. A one-dimensional profile with constant veering is given by Emeis et al. (2007, Sec. 3; Eq. 3.1-3.19).

Gryning et al. (2007) present an extension of the wind-speed profile beyond the surface layer using a neutral reference profile and a stability correction; Kelly and Gryning (2010), based on a probabilistic representation of stratification, develop a model for the long-term mean wind speed in the ABL and compare this with observation at different sites; Kelly and Troen (2016) demonstrate the effect of such improved model for wind-energy applications. In consideration of the large scale separation in geophysical flow, the rotation of the wind in the surface layer is often assumed negligible, and above investigations merely focus on the wind speed; that means, the veering of the wind with height is not described and there is little knowledge on the profile of the span-wise velocity component and the precise shape of the hodograph in the limit of a truly neutral Ekman boundary layer. A climatology of wind turning in the ABL is given by Lindvall and Svensson (2019)

79 Klein et al. (2021) use a statistical turbulence modelling approach that yields a
80 two-component velocity profile, but they also find that the exact representation of
81 turning is challenging.

82 Ekman-layer models are roughly based on Ekman's seminal 1905 paper in
83 combinations with additional assumptions. One option is a prescribed profile shape
84 for eddy viscosity (Ellison (1955)), another are two-layer models of the ABL that
85 take into account rotational effects at higher altitudes, for instance when the wind
86 speed needs to be evaluated at heights on the order of 100 – 200 m, a particular
87 concern when it comes to wind-power forecasting (Etling 2002; Emeis 2018; Optis
88 et al. 2014). Despite rotational effects being considered, the formulation of these
89 models for the outer layer and analysis of their performance primarily focuses
90 on wind speed. Still, in 2018, Jiang et al. recognized that the outer part of the
91 Ekman boundary layer receives less attention in comparison with the surface layer
92 and study the neutral problem by Large-Eddy simulation (LES). They focus on
93 the wind speed and find an extended logarithmic layer when considering the wind
94 speed instead of the shear-aligned component, and they eventually demonstrate
95 by means of an analytical model that this vertical extension of the logarithmic
96 layer may be explained by a transfer of stress to the span-wise velocity component
97 where it is assumed that the shear vector $\tau(z)$ and stress vectors $(\partial_z U, \partial_z V)$ are
98 aligned.

99 More recently, Ghannam and Bou-Zeid (2021) treated the horizontally av-
100 eraged momentum budget to show that departures from shear-alignment in the
101 vicinity of the surface result in an integral of the wind veer (α_M in their notation)
102 over the height to very high accuracy ($\int_{z_0}^H \sin \alpha_M$ in their notation; their Eq. (16)).
103 Classic surface-layer similarity is recovered when the angle α_M does not depend
104 on height, i.e., the wind veer is constant across the surface layer. If, however, the
105 wind veer depends on height, the profiles of stress and mean velocities depart from
106 the scalings implied by classic surface-layer similarity.

107 Turbulent Ekman flow is considered here as a conceptual model of the homo-
108 geneous, stationary ABL over a flat surface under neutral stratification. Universal
109 profiles of the wind vector for turbulent Ekman flow not only are a well-described
110 limit for theoretical exploration or higher-order approaches taking into account
111 possible effects of stratification, roughness or other physical complications encoun-
112 tered in the real geophysical system. While, on first sight, the study of such a
113 strongly idealized case appears as an academic problem, it contains the essence
114 of surface similarity as it is used in most atmospheric models, be it conceptual
115 or numeric ones. More complex accounts generally refer to the homogeneous sta-
116 tionary problem as a base state: (i) Roughness is commonly incorporated by a
117 linear transformation of vertical scale involving the roughness parameter z_0 and
118 for larger roughness also a displacement height (Monin and Yaglom 1975; Jacobs
119 and Van Boxel 1988; Högström 1988); (ii) Stability can be accounted for by a
120 linearization around the neutrally stratified profile (Monin 1970; Monin and Ya-
121 glom 1975; Högström 1988, 1996; Sakagami et al. 2020); (iii) Non-stationarity in
122 the pressure-gradient forcing can be accounted for by a linear damped-oscillator
123 approach around the base state (Momen and Bou-Zeid 2016); (iv) Barotropic and
124 baroclinic effects on the velocity profile require to consider the height-dependence
125 of the veer and stress misalignment (Momen et al. 2018; Ghannam and Bou-Zeid
126 2021). Furthermore, such a solution can serve as better initial condition for numer-

127 ical simulation of the flow, to minimize the length of initial transient periods, or
 128 as benchmark for turbulence closures that can be tuned to reproduce the neutral
 129 limit case.

130 Despite the strong simplifications implied by our choice of set-up, there is no
 131 straightforward approach to solving this well-defined problem. Large-Eddy simula-
 132 tion not only needs to be tuned for the surface shear stress and veering angle, but
 133 it also relies on sub-grid closures that commonly assume alignment of the turbu-
 134 lent stress with gradients. This pre-requisite is not fulfilled when the wind rotates
 135 with height. Esau (2004) investigated the representation of the Ekman boundary
 136 layer by dynamical subgrid closures and Zikanov et al. (2003) proposed a closure
 137 for the wind profile using a linearized representation of the eddy viscosity. Despite
 138 advances in analysis of this simplified set-up (Jiang et al. 2018), there is yet insuf-
 139 ficient understanding for a quantitative generalization of the results to arbitrary
 140 external forcing (manifest in variation of the Reynolds number) – and indeed the
 141 fundamental questions pertaining to such relatively simple dynamics of turbulence
 142 are not reflected in the research on LES for the ABL over the past 50 years (Stoll
 143 et al. 2020).

144 At the same time, an increasing amount of high-quality and high-resolution
 145 data from turbulence-resolving approaches is emerging due to recent advances in
 146 high-performance computing and its application to geophysical problem sets; the
 147 geophysical range of scale separation, however, is—and it will remain so for the
 148 foreseeable future—out of reach for such simulation (Dimotakis 2005). Here, the
 149 routinely employed concept of Reynolds-number similarity can help. It postulates
 150 the existence of *fully developed turbulence* believed to occur for a sufficiently large
 151 but finite Reynolds number (Barenblatt and Goldenfeld 1995). (Already in 1998,
 152 this in fact lead Moin and Mahesh to the question *how high a Re is high enough?*)
 153 Certain statistics of fully developed turbulence, such as dissipation (Dimotakis
 154 2005) or profiles of mean velocity (Barenblatt 1993), become independent of the
 155 Reynolds number when appropriately scaled; other statistics, such as the near-
 156 wall maximum in velocity fluctuation depend on Re (Baars and Marusic 2020)
 157 and externality of the flow may exert an impact on near-wall scaling (da Silva
 158 et al. 2014). It appears that for certain statistics in Ekman flow, fully-developed
 159 turbulence is reached with the Reynolds numbers that became possible due to an
 160 increase of computing capabilities over the past decades.

161 This paper exploits the robust features of mean velocity profiles from direct
 162 numerical simulation across a range of Reynolds numbers to formulate both the
 163 streamwise and span-wise components of the mean velocity vector as a function
 164 of the Reynolds number.

165 2 Problem formulation and numerical approach

166 We consider here incompressible, turbulent Ekman flow, that is, the turbulent flow
 167 over a flat rotating plate, as a physical model for the truly neutral ABL. The f-
 168 plane approximation is applied such that rotation only acts on horizontal velocity
 169 components; we thus neglect rotational effects on the horizontal components of
 170 velocity and dynamical effects due to latitudinal variation of the rate of rotation.

171 2.1 Notation and governing equations

172 The dimensional velocity vector of the numerical simulations is $\underline{U} = (U_1, U_2, U_3) =$
173 (U, V, W) over the coordinate system $Oxyz$, where an approximate alignment (plus/
174 minus few degrees) of the direction Ox with the surface shear stress is achieved. We
175 consider velocity profiles only, i.e. all velocities are averaged over horizontal planes
176 and in time, that is, they correspond to an Ensemble average. The coordinate Oz
177 points away from the wall, and Oy points in the span-wise direction normal to
178 Oxz . For analysis of the results, we use two coordinate systems that are (i) exactly
179 aligned with the surface shear stress

$$\underline{\tau}_{\text{sfc}} = \begin{pmatrix} \tau_x \\ \tau_y \\ \tau_z \end{pmatrix} = -\rho\nu \left(\frac{\partial U}{\partial z} \hat{e}_x + \frac{\partial V}{\partial z} \hat{e}_y \right) \quad (1a)$$

180 and labelled by an upper index α as in \underline{U}^α for the velocity vector, and (ii) the
181 coordinate system aligned with the free-atmosphere geostrophic wind labelled by
182 an upper index G as in \underline{U}^G . We denote the square root of the modulus of surface
183 shear, the surface friction, by

$$u_* = \sqrt{\frac{\|\underline{\tau}_{\text{sfc}}\|}{\rho}} \quad (1b)$$

184 and let $Z_* = G/u_*$; the surface veering angle α_* is the angle between $\underline{\tau}$ and the
185 geostrophic wind

$$\alpha_* = \sphericalangle(\underline{G}, \underline{\tau}_{\text{sfc}}). \quad (1c)$$

186 Analogously, we denote the height-local veering of the wind $\alpha(z) = \sphericalangle(\underline{G}, \underline{U}(z))$,
187 where $\underline{G} = (G_1, G_2, 0)$ is the geostrophic wind vector.

188 We consider the incompressible Navier–Stokes equations for the three velocity
189 components on the f-plane in a framework that is governed by (i) geostrophic wind
190 magnitude $G = \sqrt{G_1^2 + G_2^2}$, (ii) Coriolis parameter f (representing the angular
191 rotation), and (iii) kinematic viscosity ν . In absence of external variability, this
192 system converges to a statistically steady state in the sense that flow statistics
193 do not depend on time; and this state is defined by a Reynolds number, the only
194 non-dimensional parameter that governs the system. We use the geostrophic wind
195 as velocity and the Coriolis parameter f as time scale for the non-dimensional
196 framework. This implies the Rossby radius $A_{\text{Ro}} = G/f$ as length scale, such that
197 one Reynolds number governing the problem reads as

$$\text{Re}_A = \frac{GA_{\text{Ro}}}{\nu}. \quad (2)$$

198 The scales used in defining Re_A are of limited relevance for description of the
199 turbulent flow state. The turbulence scale separation in a wall-bounded flow is
200 commonly characterized by the friction Reynolds number (Jiménez 2012):

$$\text{Re}_\tau = \frac{u_* \delta}{\nu} = \delta^+ = \frac{\text{Re}_A}{Z_*^2}, \quad (3)$$

201 where $\delta = u_*/f$ and we use a superscript '+' to denote normalization by inner
 202 turbulence scales (u_*, ν) . The outer normalization (with respect to the boundary-
 203 layer depth δ and velocity u_*) is denoted by a superscript '−', i.e. $z^- = z/\delta$.
 204 Another common measure of scale separation is the Reynolds number

$$\text{Re}_D = \frac{GD}{\nu} \quad (4)$$

205 defined by the laminar Ekman layer thickness $D = \sqrt{2\nu/f}$.

206 The governing equations non-dimensionalized by G , f , and A_{Ro} read as

$$\frac{\partial u_i}{\partial t} = \frac{\partial \pi}{\partial x_i} - u_j \frac{\partial u_i}{\partial x_j} + \epsilon_{i2j}(u_j - g_j) + \frac{1}{\text{Re}_A} \frac{\partial^2 u_i}{\partial x_j^2} \quad (5a)$$

$$\frac{\partial u_j}{\partial x_j} = 0, \quad (5b)$$

207 where $u_i = U_i/G$ are the non-dimensional components velocity, π is non-dimen-
 208 sional pressure, $g_j = G_j/G$ are non-dimensionalized components geostrophic wind
 209 (with $g_1^2 + g_2^2 = 1$ by construction), and ϵ is the Levi–Civita tensor. These equations
 210 are solved inside a bounded cube of size $L_x \times L_y \times L_z$ with periodic boundary condi-
 211 tions in the lateral (streamwise and spanwise) directions, a no-slip–no-penetration
 212 boundary at $z = 0$, and a no-penetration, free-slip boundary at $z = L_z$.

213 2.2 Numerical simulations

214 The problem is solved numerically by tLab¹, an open-source tool-suite to simulate
 215 and analyze turbulent flows. We use here a fourth-order–five-step Runge–Kutta
 216 integration and sixth-order compact schemes for spatial derivatives in all direc-
 217 tions. The incompressibility constraint is enforced by a fractional step approach
 218 where the Poisson equation for the pressure field is solved to machine accuracy
 219 using a combined spectral/compact approach as described in Mellado and Ansorge
 220 (2012).

221 Simulations used here are shown in Tab. 1. We extend an existing set of simula-
 222 tions for $\text{Re}_A \in \{125\,000; 281\,250; 500\,000\}$ (gray shading; cf. Ansorge and Mellado
 223 2014, 2016) by new simulations at higher Reynolds numbers up to $\text{Re}_A = 1.28 \times 10^6$
 224 with a horizontal domain extent up to 3.3×10^4 viscous units. In total, this yields
 225 one order of magnitude variation in terms of the scale separation in the boundary
 226 layer.

227 3 Scaling behavior of the flow for Re_τ up to 3000

228 The generalization of profiles to arbitrary Reynolds numbers requires sufficient
 229 scale separation in the simulations, not only to quantify the effect of the Reynolds
 230 number on low-order flow statistics, but also to assess the corresponding rate-of-
 231 change to eventually allow for an extrapolation of the findings. While the simula-
 232 tions previously available (gray shading in Tab. 1) give confidence in a first-order

¹ <https://github.com/turbulencia/tlab>

Table 1 Direct numerical simulation data sets used in this work. Re_A and Re_D refer to the Reynolds number defined in terms of the Rossby radius Λ and Ekman-layer thickness D respectively. L_{xy} is the domain size in the stream- and span-wise direction. The grid is given by the number of grid points in the stream-wise (N_x), span-wise (N_y) and vertical (N_z) directions respectively. The resolution in the span-wise and stream-wise directions are given as Δx^+ and Δy^+ . The grid in the vertical is stretched, and resolution at the wall is given by Δz^+ .

Re_A	Re_D	L_{xy}/Λ	$N_x \times N_y \times N_z$	Δx^+	Δy^+	$\Delta z^+ _{z=0}$
125 000	500	1.08	$2048 \times 2048 \times 192$	4.1	4.1	1.05
281 250	750	1.08	$3072 \times 3072 \times 384$	5.6	5.6	1.60
500 000	1 000	1.08	$3072 \times 6144 \times 512$	9.3	4.7	1.14
845 000	1 300	0.54	$2560 \times 5120 \times 640$	8.9	4.5	0.99
1 280 000	1 600	0.54	$3860 \times 7680 \times 960$	8.6	4.3	1.00

Table 2 DOIs and reference to the openly accessible data set at refubium repository

Re_D	DOI	Reference
500	10.17169/refubium-42505	Ansorge (2024a)
1000	10.17169/refubium-42507	Ansorge (2024b)
1300	10.17169/refubium-42508	Ansorge (2024c)
1600	10.17169/refubium-42509	Ansorge (2024d)

representation of the turbulent problem, the estimation of higher-order effects such as the dependency of the Reynolds number requires a broader scale separation that is made available by the two new simulations at increased Reynolds number (cf. Tab. 1). Data at such scale separation has been obtained previously (cf. Spalart et al. 2008, 2009), but we also need high confidence with respect to the convergence of simulation data for slow oscillations and with respect to sampling convergence, which translates to two further requirements on the data: First, data should be free of artifacts from long-term oscillations across the vertical extent of the domain—primarily, simulations should be free of effects originating from the inertial oscillation; this is achieved here by replacing the mean value of the three-dimensional velocity fields by the time mean over a whole inertial oscillation. Second, high accuracy is also needed in terms of the statistical convergence of averages, bulk measures and large-scale structures; this requires a domain size $L_x > \mathcal{O}(\delta_{95})$. We use here $L_x = L_y = 1.08\Lambda$ for cases with $Re \leq 1000$ and $L_x = L_y = 0.54\Lambda$ for $Re \geq 1300$ which corresponds to $L_x/\delta_{95} \approx 25$ for $Re_D = 500$ and $L_x/\delta_{95} \approx 18$ for $Re_D = 1300$.

Bulk parameters of the simulations are given in Tab. 3. The surface stress is characterized by u_* and α_* in relation to the geostrophic wind vector and discussed in more detail as the drag law below in Sec. 4.1 (we find the expected slight decrease of u_*/G and α_* with increasing Re). The boundary-layer height estimated from the 95% stress reduction, δ_{95} , is around 0.6δ to 0.66δ . Interestingly, the integrated TKE $\int_0^\delta edz$ stays constant when normalized by the friction velocity u_* while the integrated dissipation $\int_0^\delta edz$ exhibits inviscid scaling when normalized by the magnitude G of the geostrophic wind. (TKE and dissipation normalized as $fG^{-3} \int edz$ and $u_*^{-3} \int edz$, exhibit substantial dependence on Re for the variation of u_* .) This indicates that the bulk dissipation is governed by the forcing G —irrespective of Re . Changes in Re , however, affect the level and organization of turbulence, and the parameter representing this dependency is the friction veloc-

Table 3 Bulk characterization of the simulations for different Reynolds numbers Viscous Reynolds number Re , friction Reynolds number Re_τ , friction velocity u_* , surface veering angle α_* , normalized boundary layer depth δ_{95}/δ , inner normalization of vertically integrated TKE, outer normalization of vertically integrated dissipation.

Re	$\delta^+ = \text{Re}_\tau$	u_*/G	α_*	δ_{95}/δ	$f u_*^{-3} \int_0^\delta \epsilon dz$	$G^{-3} \int_0^\delta \epsilon dz$
500	479	0.0619	25.5	0.66	0.88	1.31
750	886	0.0561	21.0	0.65	0.90	1.34
1000	1403	0.0530	18.8	0.62	0.92	1.30
1300	2122	0.0501	17.9	0.59	0.85	1.24
1600	2978	0.0482	17.2	0.61	0.91	1.21

ity u_* which describes the turbulence production processes in the surface layer, in particular in the buffer layer.

Velocity profiles in inner units ($U^{\alpha+}(z^+)$, Fig. 1a) and outer units ($U^{\alpha-}(z^-)$, Fig. 1b) are in accordance with previous work (Coleman et al. 1992; Spalart et al. 2008, 2009; Ansorge and Mellado 2014; Ansorge 2019): The profiles of the shear-aligned streamwise velocity component are well-collapsed for $\text{Re}_D > 500$ below $z^- \approx 0.15$ (circles in Fig. 1a); the case with $\text{Re}_D = 500$ is only transitionally turbulent and there is no distinct inner-outer scale separation. The logarithmic law is appropriate for $50 < z^+ < 0.15\text{Re}_\tau$, where $z^+ = \text{Re}_\tau z^-$. While the profiles $U^{\alpha+}(z^+)$ diverge between different Re beyond $z^- = 0.15$, the corresponding profiles of the velocity deficit ($U^{\alpha+}(z^-) - G_1^\alpha$) agree closely, irrespective of Re . This illustrates the inner–outer scale-duality in this external flow with inner scaling being appropriate in the inner layer and outer scaling in the outer layer. Also in the outer layer of the flow, u_* (and not the magnitude of the geostrophic wind G) governs the inviscid normalization, i.e. a scaling independent of the Reynolds-number.

No collapse is found for the profiles of spanwise velocity when considered in inner units, $V^{\alpha+}(z^+)$. When normalized in outer units, the deficit profiles of spanwise velocity ($V^{\alpha+}(z^-) - G_2^\alpha$) agree well beyond $z^- \approx 0.3$. This is a much higher level in comparison with the streamwise component that collapses also within the overlap layer, i.e. much closer to the surface (circles in Fig. 1b). The value of $V^{\alpha+}(z^-) - G_2^\alpha$ is sensitive to the wind veering for $z \rightarrow 0$ as—for use of the shear-aligned component—it has to approach the value $-G_2^\alpha = |G| \sin \alpha \neq 0$ in view of the no-slip boundary condition. While low-Re effects appear to be present for $\mathcal{O}(\text{Re}) < 10^3$, the spanwise component converges to an Re -independent limit within the range of scale separation considered here, i.e.

$$G_2^\alpha/u_* = Z_* \sin \alpha \rightarrow \text{const. for } \text{Re} \rightarrow \infty, \quad (6)$$

which has indeed already been found by Spalart (1989), who estimates the constant from an integral relation.

The viscous stress

$$S_{\text{visc}} = \nu \sqrt{\left(\frac{\partial U}{\partial z} \right)^2 + \left(\frac{\partial V}{\partial z} \right)^2} \quad (7a)$$

exhibits universal scaling when considered as $S_{\text{visc}}^+(z^+)$ (Fig. 2a); this normalization is also appropriate in the outer layer where the viscous stress is, however,

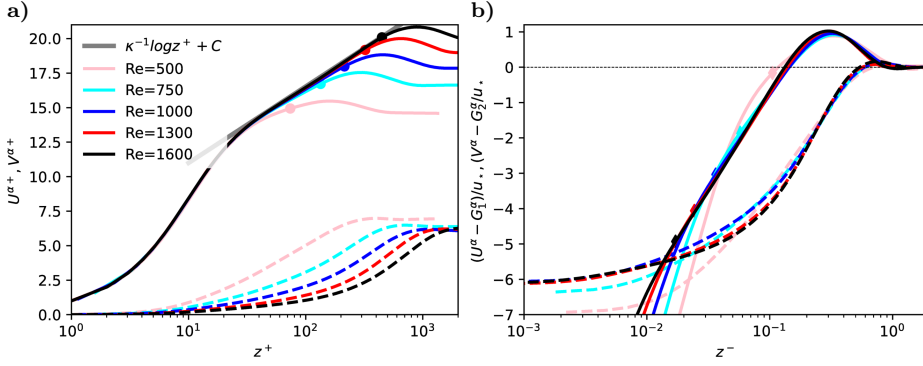


Fig. 1 a) Shear-aligned velocity profiles in inner units; circles mark the height $z^- = 0.15$; b) Shear-aligned velocity deficit in outer units; diamonds mark the grid point closest to the height $z^+ = 50$

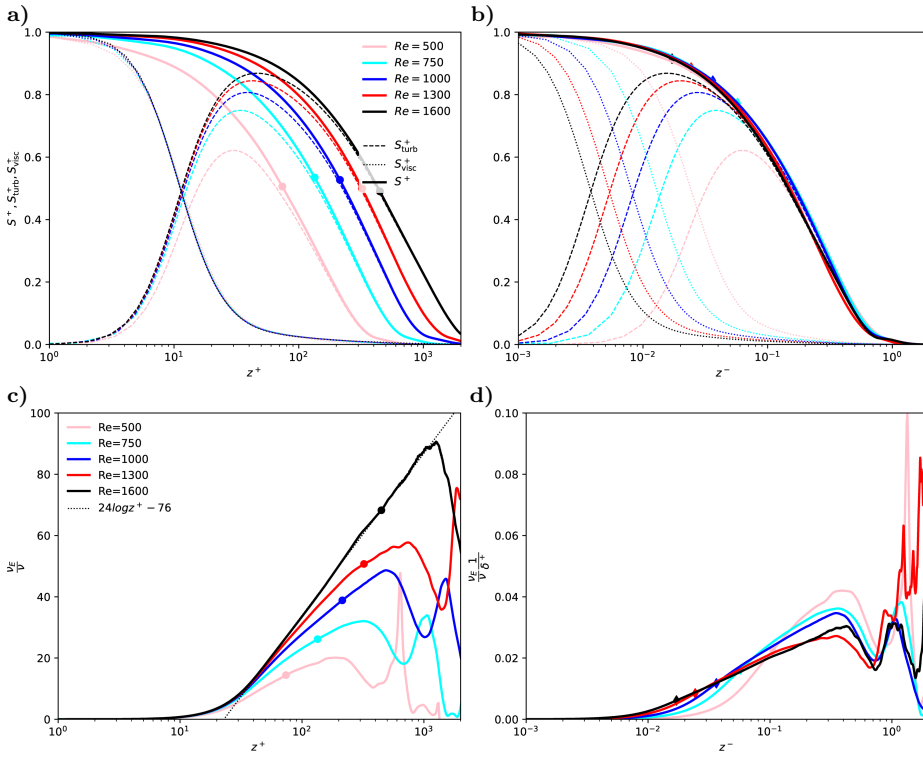


Fig. 2 a-b) Profiles of the turbulent stress S_{turb}^+ (dashed), the viscous stress S_{visc}^+ (dotted), and the total stress, $S^+ = S_{\text{visc}}^+ + S_{\text{turb}}^+$ (solid) as a function of inner height (a) and outer height (b). c-d) Normalized eddy viscosity ν_E (solid) plotted versus inner height (c) and outer height (d). (c) uses inner normalization; (d) uses normalization by $\nu\delta^+$ which approximately collapses data in the outer layer. Different colors are for different Reynolds numbers (cf. Tab. 1). Circles in (a) and (c) denote the height $z^- = 0.15$, diamonds in (b) and (d) are for $z^+ = 50$ as in Fig. 1

292 small. Small deviations from the universal profile are observed for the smallest
 293 Reynolds number $\text{Re} = 500$; we attribute these to low-Re effects in the only trans-
 294 transitionally turbulent flow ($\text{Re}_\tau = 479$). In contrast to the viscous stress, the total
 295 stress follows outer normalization, i.e. $S^+(z^-)$ is universal; a discrepancy in the
 296 inner layer does not occur as the total stress is approximately constant in the
 297 viscous and buffer layer, and a rescaling of the height would have no effect there;
 298 above, outer scaling is appropriate for the well-established dynamics in the over-
 299 lap region of inner and outer layer. This, however, implies a mixed scaling for the
 300 turbulent stress,

$$S_{\text{turb}} = \sqrt{\overline{u'w'}^2 + \overline{v'w'}^2}, \quad (7b)$$

301 where dashed quantities u' , v' , w' indicate deviations from the mean and the
 302 overbar denotes horizontal and time averaging. Indeed, S_{turb} only follows inner
 303 normalization below $z^+ \lesssim 20$ (where the turbulent contribution is negligible). In
 304 the outer layer, where $S_{\text{visc}} \rightarrow 0$, S_{turb}^+ follows outer normalization for $z^- \gtrsim 0.15$ —
 305 with increasing accuracy for larger Re and larger distance from the surface. In the
 306 overlap region, i.e. for $z^+ > 20$ and $z^- < 0.15$, the mixed scaling for the turbulent
 307 stress can be expressed as

$$S_{\text{turb}}^+(z^+, \text{Re}_\tau) = S^+(z^-) - S_{\text{visc}}^+(z^+), \quad (7c)$$

308 where $z^- = z^+/\text{Re}_\tau$.

309 The Eddy viscosity plays a crucial part when modelling profiles and the vertical
 310 transport in turbulent flow. In analogy to the Fick-law for molecular diffusion, the
 311 eddy diffusivity is the effective diffusivity that yields the turbulent transport S_{turb}
 312 based on the strain rate. For the symmetries in the flow (horizontal homogeneity,
 313 and $W = 0$), it is

$$\nu_E = \frac{S_{\text{turb}}}{\sqrt{\left(\frac{\partial U}{\partial z}\right)^2 + \left(\frac{\partial V}{\partial z}\right)^2}} = \nu \frac{S_{\text{turb}}}{S_{\text{visc}}}. \quad (8a)$$

314 The inner normalization of ν_E is obtained when dividing by the molecular viscosity:

$$\nu_E^+ = \nu_E/\nu = S_{\text{turb}}/S_{\text{visc}}. \quad (8b)$$

315 Under this normalization, the profiles of eddy viscosity collapse below $z^+ \approx 20$
 316 with a tendency towards better collapse at higher z^+ for higher Reynolds number
 317 (up to $z^+ \approx 50$ for $\text{Re} = 1600$; Fig. 2c). In the outer layer, the eddy viscosity
 318 is characterized by a distinct minimum at $z^- \approx 0.6 - 0.8$, and we find that the
 319 following mixed normalization of ν_E by the geostrophic wind and friction velocity
 320 collapses the value of ν_E at this minimum (cf. Fig. 2d):

$$\nu_E^- = \nu_E^+ \frac{1}{\delta^+} = \nu_E \frac{1}{\nu} \frac{\nu}{u_* \delta} = \nu_E \frac{f}{u_*^2}. \quad (8c)$$

321 Substantial variation of the profiles is, however observed below and above this
 322 minimum for different Re which illustrates that this normalization is probably not
 323 generally appropriate across the outer layer.

324 The organization of the flow with $\text{Re}_\tau = 2978$ is depicted in terms of the
 325 turbulence kinetic energy in Fig. 3. In vicinity of the wall, at $y^+ \approx 10$, (Fig. 3a),
 326 elongated streaks aligned with the surface shear stress dominate. Moving away
 327 from the wall, to $y^+ \approx 150$ (well within the logarithmic region), the structures are

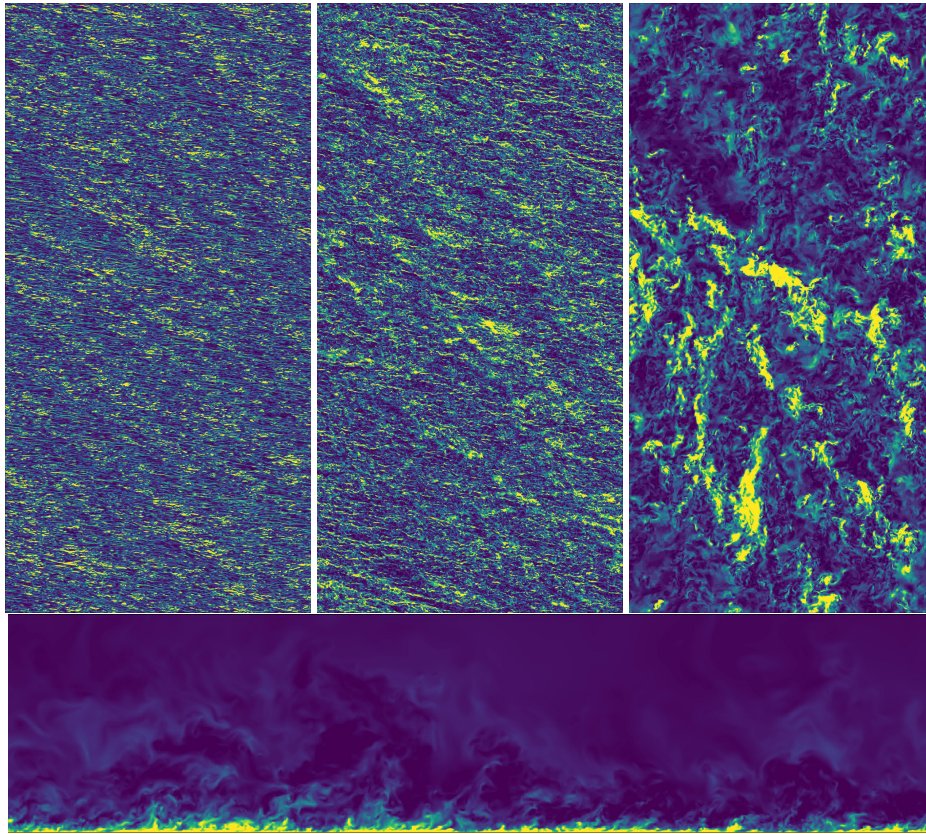


Fig. 3 Horizontal slices of turbulence kinetic energy in the Buffer layer ($i=10$), logarithmic Layer ($i=100$), and outer layer ($i=400$) of the case with $Re_\tau = 2978$; coloring between percentiles 4 and 96 of the respective image. Lower panel: streamwise–vertical intersect through the domain

328 larger and more isotropic, but they are still largely aligned with the surface shear
 329 stress. In the upper part of the outer layer, around $y^+ \approx 1000$, no clear signature of
 330 the surface veering direction is found, and intense TKE structures (bright yellow)
 331 are organized on a large spatial scale with weaker eddies (greenish structures) and
 332 quiescent regions in between.

333 4 A universal velocity profile for the turbulent Ekman layer

334 We now turn to the formulation of a general velocity profile that is fully determined
 335 by the only parameter of the idealized problem, namely a Reynolds number repre-
 336 senting the scale separation or geometric size of the problem. This precludes, first,
 337 a drag law wherewith we begin this section (4.1). Based on the scaling arguments
 338 put forward in Sec. 3, we then develop, second, a formulation of the wind vector
 339 in the Ekman layer (Sec 4.2). Finally, we come up with a separate formulation of
 340 the, third, stream-wise and, fourth, span-wise velocity components in the overlap
 341 and inner regions of the flow.

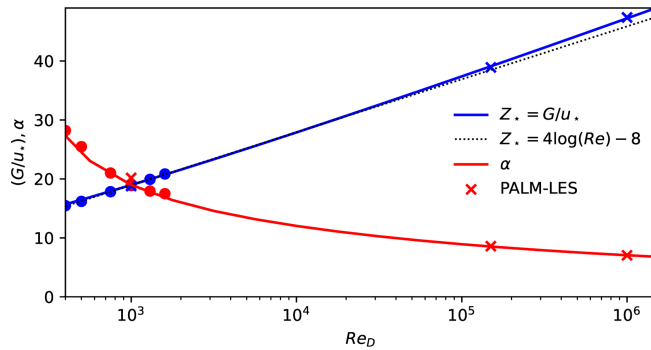


Fig. 4 Variation of geostrophic drag, Z_* , and surface veering, α_* , with Reynolds number according to the theory by Spalart et al. (1989) and as estimated from DNS data

342 4.1 Drag-law

343 A drag-law for Ekman flow determines—as a function of Reynolds number alone—
 344 the surface drag. This can be formulated by the normalized surface friction, u_*
 345 (Eq. (1b), also termed geostrophic drag), and the direction of surface shear stress,
 346 α_* (Eq. (1c), also termed wind veer). A non-zero veering of the wind is a rather
 347 special case in comparison with most turbulent flows considered in an engineering
 348 context, and it confronts us with a situation where the most appropriate coordinate
 349 system for analysis (namely that aligned with the surface shear stress) is a priori
 350 unknown. We compare our DNS data against a semi-empirical drag-law based on
 351 integral consideration (Spalart 1989) and find, as demonstrated in previous work
 352 (Ansorge and Mellado 2014), excellent agreement in the range $400 < \text{Re} < 1600$,
 353 representing a factor of 16 in variation of viscosity.

354 We also find that the solution of the transient equation involved in estima-
 355 tion of u_* for a given Reynolds number Re_D is approximated reasonably by the
 356 formulation

$$Z_* = 4 \log(\text{Re}_D) - 8 \quad (9)$$

357 which quantifies the ‘weak’ dependence of u_* on the Reynolds number as an ap-
 358 proximately logarithmic one, at least for problems with a scale separation on the
 359 order that is relevant to geophysical problems ($Re_D < 10^8$).

360 4.2 Profile in the Ekman layer

361 Formulations for the outer layer that take into account the rotation (and thus
 362 deviation from the channel-flow analogy) need to be matched to the framework of
 363 surface similarity. A smooth transition from the inner layer to the Ekman layer,
 364 where the wind is characterized by a turning of its mean direction, is not eas-
 365 ily achieved. Optis et al. (2014), for instance, define an “*effective geostrophic wind*
 366 *vector that has the same magnitude of the observed surface geostrophic wind and is ro-*
 367 *tated by the angle α [their nomenclature]*” to overcome the unsteady transition when
 368 approaching the Ekman layer from below. Such rotation of the wind vector is *a*
 369 *posteriori* justified by the observational data that the model outcomes are com-
 370 compared to. This need for a connection of the two reference frames is a manifestation

371 of a mismatch in the theoretical treatment of the inner and outer layer in this
 372 rotating flow configuration.

373 The text-book solution for Ekman flow makes use of the physical boundary
 374 conditions (BCs) for the ABL (no-slip at the bottom and geostrophic wind in the
 375 free atmosphere) and a constant eddy viscosity. Specifying the boundary conditions
 376 at top and bottom eliminates one mode of the analytical solution, and it determines
 377 the magnitude of the spiral. In doing so, one has to assume that the solution
 378 is appropriate across the entire ABL, which is not the case: The dynamics put
 379 forth by Ekman in 1905 are not appropriate in the surface layer of the ABL;
 380 better approximations exist for the logarithmic, buffer, and viscous sublayers. In
 381 view of this situation, we use an adapted Ekman spiral that does not enforce the
 382 boundary conditions at the surface but at a different height. This is achieved by
 383 considering the Ekman spiral only in the Ekman layer, thus giving way for the
 384 well-established logarithmic and viscous-layer profiles in the lower surface layer.
 385 Based on the derivation in App. A.1, this profile is given by

$$\frac{1}{G} \begin{pmatrix} U_{ek} \\ V_{ek} \end{pmatrix} = \begin{pmatrix} 1 \\ 0 \end{pmatrix} + e^{-z_{ek}} \left[a_{ek} \begin{pmatrix} -\cos z_{ek} \\ \sin z_{ek} \end{pmatrix} + b_{ek} \begin{pmatrix} \sin z_{ek} \\ \cos z_{ek} \end{pmatrix} \right]. \quad (10a)$$

386 with $z_{ek} = \delta_{ek}(z^+ - s_{ek})$. The right-hand-side consists of two modes with magnitude
 387 a_{ek} and b_{ek} shifted by $\pi/2$ with respect to each other. In the classic case, the second
 388 mode governed by b_{ek} is incompatible with the surface boundary condition. While
 389 this is not the case here for the general form of the profile, the phase shifts can also
 390 be captured by the parameter s_{ek} , and we stick with to a single-modal approach,
 391 i.e., we let $b_{ek} = 0$.

392 This single-modal solution is characterized by three parameters, (i) an Ekman-
 393 layer depth scale δ_{ek} , (ii) the magnitude parameter of the spiral a_{ek} , and (iii) a
 394 zero-crossing point for the velocity s_{ek} . The effects of varying these parameters
 395 are illustrated in Fig. 5 where the classic Ekman solution is recovered by setting
 396 $a_{ek} = 1$, $s_{ek} = 0$ and $\delta_{ek} = \sqrt{2\nu/f}$. These parameters are *a priori* unknown as
 397 they need to conform to the turbulent state of the boundary layer; we use our
 398 DNS data to arrive at best estimates for them.

399 **The Ekman-layer depth scale δ_{ek}** is fundamentally defined by the eddy vis-
 400 cosity. However, we have seen in Section 3 that a characteristic value for the
 401 eddy diffusivity is not easily obtained for its strong dependence on the Reynolds
 402 number and distance from the surface. We therefore resort to the physical man-
 403 ifestation of the eddy diffusivity in an Ekman layer, and use the boundary layer
 404 depth $\delta_{ek} = 0.66\delta \times 2\pi$. For the relation $\delta_{ek} = \sqrt{2\nu_{ek}/f}$, this yields $\nu_{ek} \propto u_*^2/f$ in
 405 accordance with the observations in Sec. 3 (Eq. 8c).

406 **The magnitude parameter of the Ekman spiral**, a_{ek} , defines the super-
 407 geostrophic maximum of the wind profile aloft the logarithmic layer. Our simu-
 408 lations suggest this maximum of the velocity deficit remains constant when nor-
 409 malized by u_* as shown in Fig. 6. The numerical value of a_{ek} is estimated from
 410 visual comparison, and we find $a_{ek} = 8.4u_*$; while this appears rather large, it is
 411 pre-multiplied by $e^{-z_{ek}}$ which has already decreased to $\mathcal{O}(0.1)$ at the height of this
 412 maximum. This choice ascertains that the velocity deficits $U/u_* - Z_*$ and $V/u_* - Z_*$
 413 do not depend on the velocity scale u_* , but only on G as

$$U_{ek}/u_* - Z_* \propto a_{ek}Z_* = 8.4G. \quad (11)$$

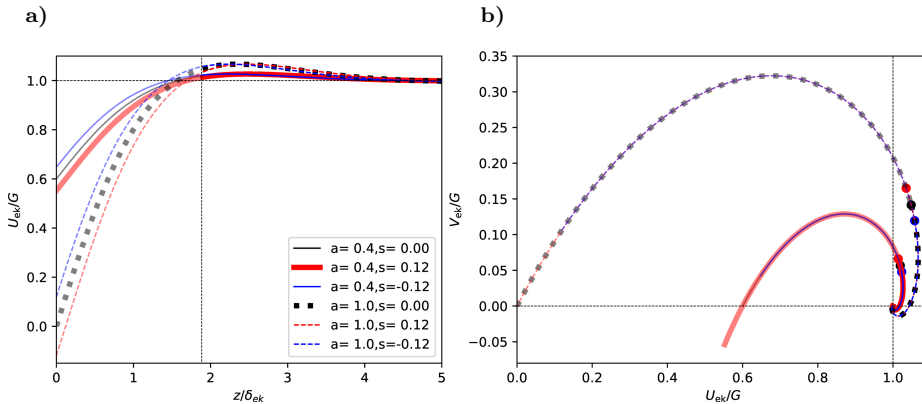


Fig. 5 a) Generalized Ekman-profile of the geostrophic-aligned component U_{ek} . b) Hodograph for the geostrophic-aligned and pressure-gradient aligned components U_{ek} and V_{ek} . Thick, black dashed line shows the classic solution. The height corresponding to $z^- = 0.30$ is marked by the dashed line in panel (a) and by filled circles in panel (b). The hodograph and profiles above this reference height are shown as solid lines, below as opaque line.

414 The offset parameter s_{ek} defines the zero-crossing height of the profile (in
 415 contrast to δ_{ek} , which determines the thickness across which the wind veering
 416 takes place). Physically, this offset can be understood as the height at which the
 417 surface was located assuming a perfect Ekman flow down to the surface. As this
 418 is not the case, and gradients are steeper in the highly turbulent boundary layer
 419 flow encountered when approaching the surface, the offset is smaller than zero (the
 420 fully turbulent boundary layer is actually thinner than an Ekman layer would be).
 421 From our DNS data, we estimate $s_{ek} = -0.12$.

422 In summary, the outer layer of Ekman flow is characterized by a turning of
 423 the wind velocity and the super-geostrophic maximum that is sustained by mo-
 424 mentum convergence at the inflection point of the velocity profile. The super-
 425 geostrophic maximum of streamwise velocity and a secondary minimum aloft the
 426 bulk-turbulent part of the boundary layer are well-described by a classic Ekman
 427 spiral with adapted boundary conditions and a shift in reference height. Corre-
 428 sponding profiles are shown in comparison with data from three DNS runs in
 429 Fig. 6. The idealized profiles capture the secondary minimum and convergence to
 430 the geostrophic equilibrium in the non-turbulent flow very well.

431 4.3 Streamwise velocity component

432 Well-established theories exist for the streamwise velocity profile, which in non-
 433 rotating flows is aligned with the surface shear stress due to the geometry. These
 434 theories cover various regimes based on their distance from the wall and the relative
 435 influence of viscosity, turbulence, and interaction with the outer flow region, with
 436 the logarithmic law for the mean velocity serving as a central reference point.

437 In immediate vicinity to the surface, local turbulent mixing cannot occur for
 438 the no-slip/no-penetration boundary condition, and the mean velocity is described

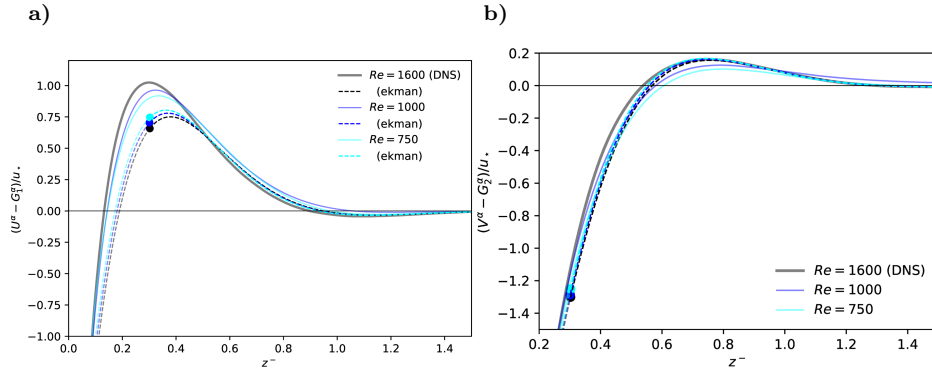


Fig. 6 Shear-aligned velocity deficit for the streamwise (panel **(a)**) and spanwise (panel **(b)**) components of the mean velocity U^α and V^α . Solid lines show DNS data, dashed lines the Ekman profiles U_{ek} and V_{ek} as defined in Eq. 10. Variations in U_{ek} and V_{ek} are a consequence of the normalization and related to changes in u_* and α_* among the different Re_D .

439 by a viscous profile of the form

$$U^{\alpha*+} = z^+ \quad (12a)$$

440 where the direction of the velocity points into the exact opposite direction of the
 441 wall shear stress τ . In absence of roughness elements and for small roughness
 442 ($z_0^+ < 5$), this linear regime is known as viscous sub-layer Foken (2002); Foken
 443 et al. (1978). In fact, this law of the wall has no degree of freedom given the
 444 drag, i.e. once u_* and α_* are defined. However, theoretical foundation is lacking
 445 for the exact shape of the velocity profile in the buffer layer; though crucial for
 446 turbulence production, it is commonly understood as a transition region between
 447 the linear profile at the surface and the logarithmic profile aloft. A pure blending
 448 from the linear velocity profile into the logarithmic one is, however, not reasonable
 449 as both the linear and logarithmic profile overestimate the velocity in the buffer
 450 layer. We therefore introduce a two-step correction procedure, accounting for the
 451 smaller-than linear growth beyond $z^+ \approx 5$, and assuring smooth matching with
 452 the logarithmic law at $z^+ = 40$:

$$U_{\text{inner}}^{\alpha*+} = \frac{z^+}{1 + c_1(y^+)^2} + (c_2 z^+ - a_{\text{match}}) \frac{1 + \tanh[0.2(z^+ - 22)]}{2} + c_3 e^{-c_4(z^+ - 22)^2}. \quad (12b)$$

453 We use here

$$c_1 = 0.00185; \quad c_2 = 0.195; \quad c_3 = 0.4; \quad c_4 = 0.35.$$

454 The second and third terms on the right hand side vanish for $z^+ \ll 22$, and
 455 $c_1 = 0.00185$ implies an approximately 5% correction at $z^+ = 5$ and an 18.5%
 456 correction at $z^+ = 10$. The second and third term on the R.H.S. of eq. (12b) are
 457 an empirical fit to the velocity profiles observed in the buffer layer and appear
 458 independent of the Reynolds number for the range observed here. The coefficient
 459 a_{match} , which has no effect in the viscous sublayer, is then used to match this
 460 formulation to the logarithmic law employed above.

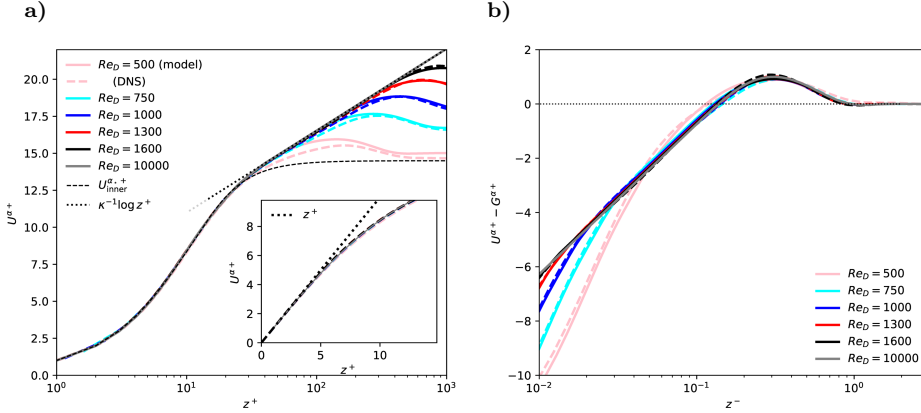


Fig. 7 Shear-aligned profiles of velocity components $U^{\alpha*+}$ in inner (left) and outer (right) units.

In the logarithmic region, we use the profile

$$U_{\log}^{\alpha*+} = \frac{1}{\kappa} \log z^+ + C \quad (12c)$$

with the von-Kármán constant $\kappa = 0.416$ and the boundary condition $C = 5.4605$.
For this logarithmic law, $a_{\text{match}} = 3.569861$ for a matching at $z^+ = 40$.

464 4.4 Spanwise velocity component

The background rotation and associated veering of the surface wind implies a non-zero profile for the span-wise velocity which challenges the conventional assumptions related to the channel-flow analogy: While the analogy with channel flow in vicinity of the wall implies that the streamwise component be zero or at least small, the veering requires a value of $V_{top} = U_G \sin \alpha_*$ in the free stream (and thus also at the top of the boundary layer if we assume that any substantial velocity gradient is confined to the turbulent part of the flow). This continuous rotation of the wind vector is conveniently visualized by velocity hodographs aligned with the outer, geostrophic flow (cf. Fig. 5b) and normalized by the geostrophic wind. The geometry of the flow and its drag imply the following for any hodograph: (i) the boundary conditions at the surface, (ii) the boundary condition at the top, and (iii) the inclination of the hodograph at the origin by the surface veering:

$$V^{\alpha*}(z = 0) = 0, \quad (13a)$$

$$\lim_{z \rightarrow \infty} V^{\alpha*} = G \sin \alpha_* \quad (13b)$$

$$\partial_{z+} V^{\alpha*+} \Big|_{z=0} = 0. \quad (13c)$$

Outer scaling of the velocity profile further implies that the velocity deficit of $(V^{\alpha*} - G^{\alpha*})/u_*$ be a universal function of the outer height z^- . In the outer region of the flow (for $z^- \mapsto 1$), $f_V(z^-)$, should govern the spanwise velocity profile, as is supported by our DNS data (Fig. 1b); above $z^- \approx 0.3$, this profile is very well approximated by the Ekman-turning derived above (Eq. (10); Fig. 6b).

482 While this deficit is a signature of outer rotation, it is inappropriate to extend this
 483 general relation to the surface where inner scales matter: On the one hand, the
 484 variation of the spanwise velocity deficit across the boundary layer (i.e. between
 485 $0 < z^- < 1$) must match the difference implied by the drag law (u_* , α_*) and the
 486 constant value of V^{α_*} around $z^- = 0.3$. On the other hand, provided the outer
 487 velocity deficit is Re independent—the Re-dependence of α_* and u_* implies that
 488 this difference cannot be constant as a function of Re. We hence ask, how does the
 489 span-wise component scale when the surface is approached? Clearly, the spanwise
 490 contribution is small in comparison with the streamwise component throughout
 491 much of the layer below $z^- \approx 0.3$. However, we cannot assume $V = 0$ if a smooth
 492 matching between the inner and outer layers shall be achieved. In this context, we
 493 first realize that the velocity deficit $(V^{\alpha_*} - G^{\alpha_*})/u_*$ approaches a Re-independent
 494 constant around $C_{V0} = Z_* \sin \alpha = 6.1$ at the surface; deviations from this constant
 495 are only found for the lowest Reynolds numbers which is in accordance with the
 496 low-Re correction suggested by Spalart (1989). This constrains the wind veer, and
 497 it quantitatively shows that the decreasing wall friction manifest in an increase of
 498 Z_* exactly compensates the decrease of wind turning measured by $\sin \alpha_*$.

499 If the difference across the boundary layer is constant (C_{V0}) vs. Re, the av-
 500 eraged gradient $\partial_{z+} V^{\alpha_*+}$ of the spanwise velocity component must decrease as
 501 $1/\delta^+$ with increasing Re_τ . Hence, it should—at a fixed height—be $V^{\alpha_*} \propto (\delta^+)^{-1}$. A
 502 profile that agrees with the constraints of the profile at the surface and exploits
 503 the dependence of V^{α_*} on δ^+ is

$$V^{\alpha_*} \frac{\delta^+}{G} = f_{V,\text{visc}}(z^+) = v_{\text{ref}} (\omega_v z^+ - 1 + \exp[-\omega_v z^+]), \quad (14)$$

504 where v_{ref} controls the magnitude of the profile and ω_v sets the height at which the
 505 profile transitions into an approximately linear one. We find excellent agreement
 506 with the DNS data for $500 \leq Re_D \leq 1600$ below $z^+ \approx 15$ with

$$v_{\text{ref}} = 18.85; \quad \omega_v = 0.2353$$

507 (cf. Fig. 8b).

508 For the adjacent surface layer, we find a log-like transition from the quasi-linear
 509 profile inner profile around $z^+ = 10$ to a linear profile with increasing Re (Fig. 8b).
 510 We model this transition by

$$f_{V,\log}(z^+) = \frac{V_{\log}(z^+)}{G} \delta^+ = a_{\log} + b_{\log} \log z^+ + c_{\log} z^+. \quad (15)$$

511 This surface-layer profile matches the inner (viscous) scaling in vicinity of the
 512 surface to the outer (Ekman) scaling above $z^- = 0.3$ when constrained by the
 513 viscous profile at the bottom and the Ekman profile at the top:

$$f_{V,\log}(z^+ = 10) = f_{V,\text{visc}}(z^+ = 10) =: v_{10} \simeq 27.3 \quad (16a)$$

$$\frac{\partial}{\partial z^+} [f_{V,\log}]_{z^+ = 10} = \frac{\partial}{\partial z^+} [f_{V,\text{visc}}]_{z^+ = 10} =: d_{10} \simeq 4.01 \quad (16b)$$

$$f_{V,\log}(z^+ = 0.3\delta^+) = V_{\text{ek}}^{\alpha_*}(z^- = 0.3)\delta^+ =: v_{03} \quad (16c)$$

514 where v_{03} is determined by $V_{\text{ek}}(0.3)$ and $U_{\text{ek}}(0.3)$ and depends on Re. Given the
 515 Ekman formulation of the velocity profile introduced in Sec. 4.2, one may express

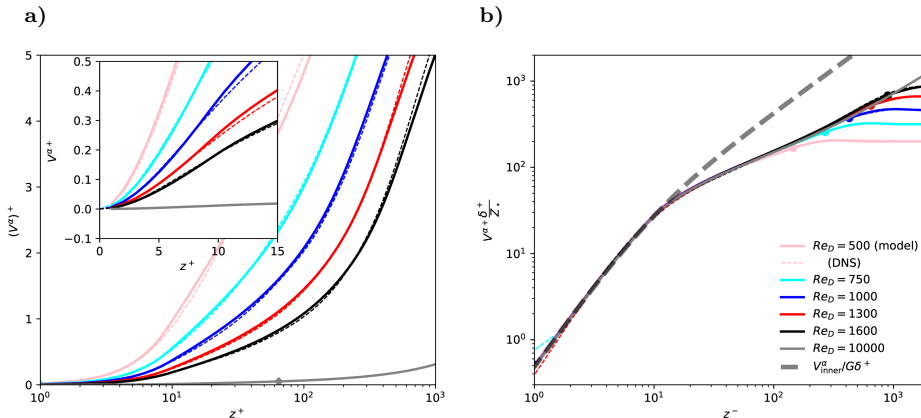


Fig. 8 Profiles of shear-aligned span-wise velocity $(V^\alpha)^+$ versus inner height. Dashed lines show DNS data, thick, opaque lines are from the semi-empirical theory developed above. Panel (a) shows standard inner normalization, panel (b) the inviscid normalization yielding a universal profile for the spanwise component of velocity in the inner layer.

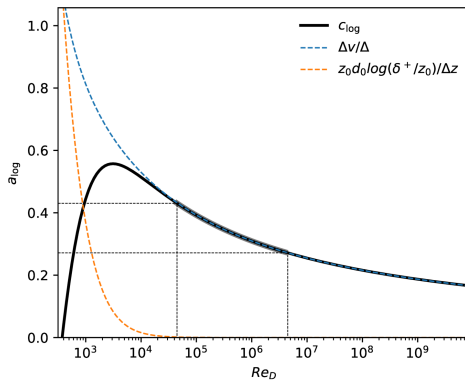


Fig. 9 Coefficients a_{\log} , b_{\log} and c_{\log} (cf. Eq. 15) as a function of the viscous Reynolds number Re_D . The approximate range of scale separation relevant for atmospheric application is found in between the dotted lines, where $a_{\log} \simeq 0$ and $c_{\log} \simeq 0.4$

516 v_{03} using the Ekman profile introduced in Sec. 4.2 together with the approximation
 517 for $u_*(Re)$ found in Eq. (9). While the Re -dependency of a_{\log} , b_{\log} , c_{\log} is small,
 518 it shows up in Fig. 1 where the normalized profiles of spanwise velocity become
 519 more convex with increasing Re . We can now quantify this effect by means of the
 520 change of c_{\log} versus Re which is shown in Fig. 9 (cf. Appendix A.2; a_{\log} and b_{\log}
 521 are then determined by the universal values of v_{10} and d_{10}).

522 4.5 Matching of the inner and outer layer profiles

523 The formulations introduced above are continuous across the transition from the
 524 inner to the outer layer. However, the requirement of smooth derivatives would
 525 over-constrain the velocity profiles and is hence not applied. This can, in particular
 526 for low or extremely high Re , cause discontinuity in the derivatives of the velocity

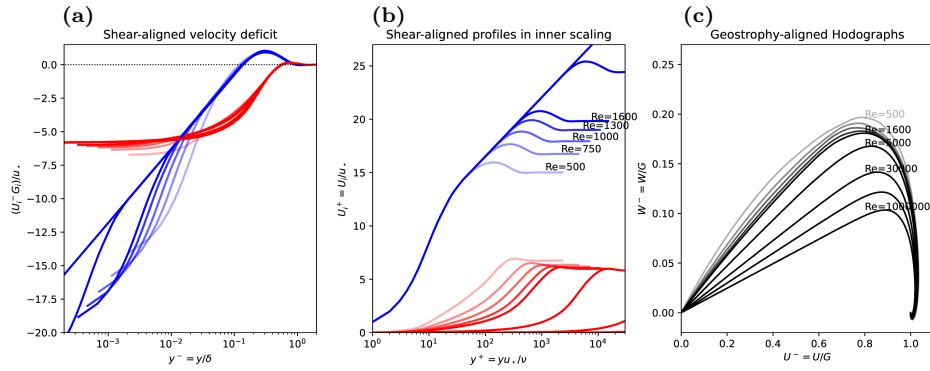


Fig. 10 (a) Velocity deficit, (b) velocity profile in shear-aligned hodographs and (c) hodograph in geostrophy-aligned coordinates. In panels (a) and (b), blue lines correspond to the streamwise component and red to the spanwise.

527 profiles around the transition from the inner to the outer layer. To avoid such
 528 artificial discontinuity, the profiles are blended by an error-function transition
 529 using a blending height $z_{blend}^- = 0.28 - 2.25\sqrt{1/Re_\tau}$ and a transition thickness
 530 $z_{trans} = 2$, such that the weighting function $\omega(z^-)$ becomes

$$\omega(z^-) = \frac{1}{2} \left[\operatorname{erf} \left(z_{trans} \log \frac{z^-}{z_{blend}^-} \right) + 1 \right], \quad (17)$$

531 hence $u_{\text{total}} = (1 - \omega) \times u_{\text{inner}} + \omega \times u_{\text{outer}}$ and similar for v .

532 The resulting velocity profiles across the entire boundary layer are shown in
 533 inner and outer scaling as well as in hodograph- view in Fig. 10. The shear-aligned
 534 velocity deficit is shown in outer scaling highlighting the universality in the outer
 535 layer. The logarithmic scaling of the streamwise component is encountered as
 536 straight blue lines in panels (a) and (b) where the extent of the logarithmic range
 537 increases with Re towards lower values of z^- and higher values of z^+ depending
 538 on the scaling. Importantly, the logarithmic region is widening for increasing
 539 Reynolds number – irrespective of the scaling. In this simple inner scaling, the
 540 spanwise velocity (which follows a mixed scaling) does not collapse but seems to
 541 depend on Re (the collapse is seen in Fig. 8). However, the velocity deficit in outer
 542 units becomes approximately universal, also across the inner layer; this reflects
 543 the compensation of reduced turning (α) by increased drag (u_*), and is consistent
 544 with the theoretical considerations discussed in 4.1.

545 The spanwise velocity at a fixed height scales approximately as Re_τ^{-1} (Sec. 4.4).
 546 However, the fraction of turning that is encountered within the inner layer of the
 547 flow amounts to about 1/3 of the total wind veer (Fig. 12a). This is because, in
 548 inner units, the inner layer grows as Re_τ which exactly compensates the reduced
 549 gradient of spanwise velocity. The hodographs show the well-known Ekman shape
 550 with the laminar profile as an outer limit and 'flatter' hodographs, corresponding
 551 to less turning, for increasing Reynolds number.

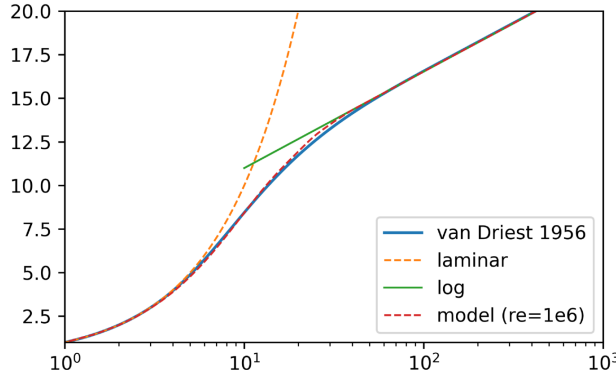


Fig. 11 Near-wall velocity profile according to the van-Driest scaling (blue, solid) in comparison with the present model (red, dashed), the viscous law of the wall (orange dashed), and the logarithmic law (green, solid)

5 Discussion

5.1 Implications for surface-layer scaling

Eq. (14) establishes a universal mixed scaling for the spanwise velocity in the viscous layer: While it requires the vertical coordinate to be expressed in inner units, the velocity itself is normalized by the geostrophic wind, and becomes inversely proportional to the friction Reynolds number $\text{Re}_\tau = \delta^+$ when considered at a fixed height. In vicinity of the surface, such mixed scaling has already been identified for higher-order statistics in convective flows (Mellado et al. 2016; Li et al. 2018), where large scales leave their signatures in vicinity of the surface. It is important to note here that, while V is a first-order statistic from a statistical perspective, the spanwise velocity is a higher-order correction term from the perspective of similarity theory and from the viewpoint of the channel-flow analogy that is routinely employed in the surface layer. Further, this is consistent with the scaling for the velocity hodograph found in Eq. (11) where the friction velocity also drops out.

In the surface layer, there is not only a mixed scaling—as we had already identified in the viscous layer—but we cannot find a universal function onto which the profiles of spanwise velocity collapse. This additional degree of freedom reflects the inner–outer matching problem for the spanwise velocity. Rather than giving a universal profile for this region, we resort here to a parametric description of the problem in terms of the function $f_{V,\log}$ determined by the parameters a_{\log} , b_{\log} , c_{\log} which can be estimated based on the above scaling considerations for any Reynolds number. We note that, once the parameter a_{\log} is known, the parameters b_{\log} and c_{\log} can be estimated solely based on $f_{V,\text{visc}}$, i.e. using the value v_{10} and d_{10} found for the viscous region of the flow. For the range of Reynolds number relevant to geophysical problems ($10^4 \lesssim \text{Re}_D \lesssim 10^6$), the variation of c_{\log} is, however, rather small.

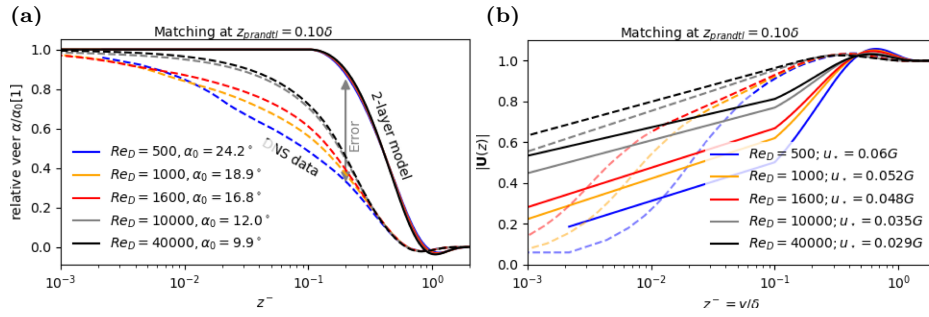


Fig. 12 Comparison of the DNS data (dashed lines) with the two-layer model proposed by Etling (solid lines) for different Reynolds number. Left panel shows the relative wind veer, right panel shows the velocity magnitude. The Etling model is calibrated by the surface veer from the DNS and the roughness parameter is chosen according to the correction factor $\exp \kappa A$ such that the total veer and velocity magnitude agree. Profiles in the buffer layer, defined here as $z^+ < 30$ are shown as opaque dashed lines as the two-layer model does not consider viscous effects.

5.2 Comparison with other theories

An alternative approach that considers viscous effects close to the surface is the van-Driest scaling (Van Driest 1956), where an exponential damping of Prandtl's mixing length is considered near the wall to yield

$$\frac{\partial u^+}{\partial z^+} = \frac{2}{1 + \sqrt{1 + (2\kappa z^+)^2} (1 - \exp[-z^+])}; \quad (18)$$

the spanwise component is zero as no rotational effects are considered. Comparing our proposed formulation for the stream-wise velocity in the inner layer to Van Driest's formulation yields later convergence of the velocity onto the logarithmic profile while, over all, it serves as an excellent model of the streamwise velocity component (Fig. 11): Notable deviations (on the order of few percent) only occur in the region $10 < z^+ < 30$, where the velocity transitions from the linear to the logarithmic profile.

For the higher layers of the ABL, the Ekman spiral is the simplest model available. When employed across the entirety of the ABL, the spiral of a turbulent Ekman layer is flattened with respect to Ekman's laminar solution, which corresponds to a reduction of the veering angle both at the surface and throughout the ABL. We, however, find that a modified version of the Ekman spiral explicitly taking into account the surface boundary condition, is a consistent model and yields excellent agreement with the velocity profiles from DNS (Sec. 4.2).

A two-layer model consolidating both the logarithmic and Ekman layer can be obtained following the arguments by Etling (2008), cf. Emeis (2018). Given a surface veering and a matching height (extent of the logarithmic layer), a formulation for the velocity profile across both the logarithmic and the outer layer is obtained. A comparison using the surface veering based on our model and a matching height of $z_{\text{prandtl}} = 0.05\delta$, which gives better results than the matching height of 0.1δ suggested by Etling (2008), is shown in Fig. 12. The overall shape of velocity magnitude is matched apart from the viscous and buffer layer

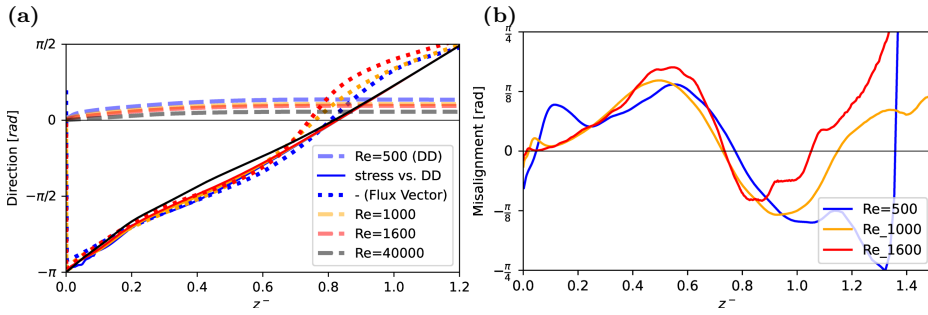


Fig. 13 Panel (a) shows the wind direction (DD) as thick dashed lines and the direction of stress relative to DD as thin solid lines, both according to our profile model. The direction of the negative flux vector ($\bar{u}'w'$, $\bar{v}'w'$) based on DNS data is shown as a dotted line. In panel (b), we plot the misalignment, i.e. the angle, between the flux vector and the shear vector, where the shear vector is defined accordingly as $(\partial_z U, \partial_z V)$.

(cf. Fig. 12b) that is neglected by the two-layer model. However, quantitative departures on the order of 10% occur across the inner layer: it turns out that the non-rotating profile, of the two-layer model in the logarithmic region yields too low overall velocity as the spanwise component contributes to the velocity across the inner layer. Deviations also occur with respect to wind direction; despite the rather low matching height, a substantial fraction of the rotation occurs within the lower part of the ABL and about 20% of the wind veer is not captured by the two-layer model. As the overall veer is given, the non-captured veer close to the surface is then compensated across the logarithmic layer. In the upper part of the boundary layer, both profiles match well.

The interpretation of flux and gradient profiles in terms of the K-theory (cf. Sec. 3, Fig. 2) suggests a certain universality in the inner layer, while a global collapse, i.e. across the boundary layer, is not obtained. While the K-Profiles concern the total stress, a consistent formulation of the turning would also require its partitioning to the individual components, i.e. the orientation of the stress vector ($\bar{u}'w'$, $\bar{v}'w'$) in the horizontal plane. If K-theory shall be used, this stress vector needs to be anti-parallel to the corresponding stress vector $(\partial_z U, \partial_z V)$. Fig. 13 shows the direction of the velocity, gradient and stress vectors across the boundary layer. It turns out that the negative stress vector with respect to the wind direction and the flux vectors (absolute) have an approximately similar direction. It appears that both rotate by about 270° ($3\pi/2$) across the boundary layer. Apart from the lower part of the Ekman layer ($0.2 < z^- < 0.7$), where there is a slight dependence on Re , the direction of stress appears to be universal, which is a consequence of the Ekman profile introduced in Sec. 4.2. However, this implies a misalignment between the flux and the stress on the order of the wind turning, and indeed Fig. 13b shows a misalignment up to $\pi/8$. This is in accordance with the expectation by (Townsend 1976, Chap. 7.18) and prevents the transfer of energy from the mean flow to turbulence at these heights, thus preventing a boundary-layer growth. While the behavior in the inner layer seems to depend on Re , there emerges universality in the misalignment across the outer layer, suggesting that a consideration of misalignment in the context of K-theory is possible when developing formulations for higher-order quantities.

636 6 Conclusions

637 We investigate the wind veer and fundamental scaling properties of the veloc-
 638 ity profiles in Ekman flow. Based on scaling considerations and direct numerical
 639 simulation spanning one decade in external separation from $Re_A = 1.25 \times 10^5$ to
 640 $Re_A = 1.28 \times 10^6$, we derive a universal formulation for the both horizontal compo-
 641 nents of the velocity profile in a stationary, smooth Ekman layer. This formulation
 642 is consistent with the DNS data and also yields reasonable results at geophysical
 643 scale separation; the logarithmic law of the mean velocity is recovered with the
 644 well-known limits and deviations towards the surface and Ekman layer. The clas-
 645 sic formulation of the Ekman layer, employing the surface boundary condition, is
 646 replaced by a modified solution that can be obtained by Ekman's system of govern-
 647 ing equations, but using different boundary conditions that are more appropriate
 648 of the actual situation encountered in the planetary boundary layer. The three pa-
 649 rameters that characterize this boundary condition are estimated based on DNS
 650 data.

651 To quantify the spanwise velocity component consistently across the boundary
 652 layer, we derive a universal scaling of the spanwise velocity component in a shear-
 653 aligned reference frame. For the *inner layer*, we find the mixed scaling

$$V^{\alpha*}/G = \frac{1}{\delta^+} f(z^+) \quad (19)$$

654 that is, the spanwise velocity normalized by the outer velocity scale is a universal
 655 function of the inner height and Friction Reynolds number $Re_\tau = \delta^+$. This scaling
 656 is derived here based on scaling considerations, and it is in excellent agreement
 657 with the DNS data available. In the outer layer, the spanwise velocity follows outer
 658 scaling, consistently with the Ekman model discussed above (Sec. 4.2).

659 Our results suggest that there is no lower limit of the turning. Hence—despite
 660 its very large scale separation / huge Reynolds number—the ABL is not in the
 661 ‘limit’ of high Reynolds number from the perspective of wind veer, but always in
 662 a regime where changes in Re impact on the vertical partitioning of rotation.

663 A Appendices
664 A.1 Laminar Ekman solution with consideration of inner layer

665 The following Ekman system is obtained by averaging the Navier–Stokes equations horizontally
 666 and over time and neglecting the turbulent transport terms (turbulence can then be considered
 667 via the eddy-viscosity concept through variations in the viscosity ν):

$$\begin{pmatrix} \partial_t U \\ \partial_t V \end{pmatrix} = \begin{pmatrix} fV & + \nu \partial_z^2 U \\ -f(U - G) & + \nu \partial_z^2 V \end{pmatrix} \quad (20a)$$

$$\Rightarrow \partial_t(U + iV) = f(V - i(U - G)) + \nu \partial_z^2(U + iV) \quad (20b)$$

668 In stationary conditions, this system is solved by

$$\dot{u}(z) = U_\infty + e^{-\gamma z} [A \cos \gamma z + B \sin \gamma z] \quad (20c)$$

$$\dot{v}(z) = V_\infty + e^{-\gamma z} [-A \sin \gamma z + B \cos \gamma z] \quad (20d)$$

669 where the constants U_∞ , V_∞ set the top boundary condition and A and B set the bottom
 670 boundary condition. The most common boundary condition for a surface Ekman layer is $A =$

671 $U_\infty = G$, $B = 0$, and $V_\infty = 0$. The lower boundary condition, however, neglects the existence
 672 of the surface layer, and it appears reasonable to define $A = cG$ where $c < 1$ is a constant that
 673 incorporates the increased shear in the surface layer. Given a 'matching height' z_{match} and
 674 normalized matching height $\xi = \gamma z_{\text{match}}$ in the upper part of the inner layer, we can match
 675 the Ekman profile to the inner layer by letting

$$\begin{aligned} u(z_{\text{match}}) &\equiv u_{\text{match}} = U_\infty + e^{-\xi} [A \cos \xi + B \sin \xi] \\ v(z_{\text{match}}) &\equiv v_{\text{match}} = V_\infty + e^{-\xi} [-A \sin \xi + B \cos \xi] \end{aligned} \quad (21\text{a})$$

676

$$\Rightarrow \begin{pmatrix} u_{\text{match}} - U_\infty \\ v_{\text{match}} - V_\infty \end{pmatrix} = e^{-\xi} \begin{pmatrix} A \\ B \end{pmatrix} \begin{pmatrix} \cos \xi & +\sin \xi \\ -\sin \xi & +\cos \xi \end{pmatrix} \quad (21\text{b})$$

$$(21\text{c})$$

677 Matching the profile at $\xi = 0$, one obtains $A = \Delta u_{\text{match}}$ and $B = -\Delta w_{\text{match}}$; and when the
 678 direction Ox is aligned with the geostrophic wind, we obtain the textbook-case $A = |\mathbf{G}|$ and
 679 $B = 0$.

680 Otherwise, choosing $B \neq 0$ allows to introduce a phase shift of the Ekman rotation with
 681 respect to the decay of the wind spiral. However, in our context, the thickness and position of
 682 the spiral can already be controlled by the eddy viscosity and an offset in ξ , here we let $B = 0$.

683 A.2 Matching the spanwise velocity profiles in the inner layer

684 The spanwise profile in vicinity of the surface is given by $V/G = f_{V,\text{visc}} \delta^+$ with

$$f_{V,\text{visc}} = v_{\text{ref}} (\omega_v z^+ - 1 + e^{-\omega_v z^+}) \quad (22\text{a})$$

$$f_{V,\log} = a_{\log} + b_{\log} \log z^+ + c_{\log} z^+ \quad (22\text{b})$$

685 Matching the profiles and gradient $z_0 = 10^+$ and the value at $z_1 = 0.3\delta^+$ yields

$$v_{\text{ref}} (\omega_v z_0 + e^{-\omega_v z_0}) = v_0 = a_{\log} + b_{\log} \log z_0 + c_{\log} z_0 \quad (23\text{a})$$

$$v_1 = a_{\log} + b_{\log} \log z_1 + c_{\log} z_1 \quad (23\text{b})$$

$$v_{\text{ref}} \omega_z (1 - e^{-\omega_z z_0}) = d_0 = \frac{b_{\log}}{z_0} + c_{\log} \quad (23\text{c})$$

686 The gradient condition implies $b_{\log} = (d_0 - c_{\log}) z_0$, and yields

$$v_0 - z_0 d_0 \log z_0 = a_{\log} + c_{\log} (z_0 - z_0 \log z_0) \quad (24\text{a})$$

$$v_1 - z_0 d_0 \log z_1 = a_{\log} + c_{\log} (z_1 - z_0 \log z_0) \quad (24\text{b})$$

$$\Rightarrow c_{\log} = \frac{\Delta v - z_0 d_0 \log z_1 / z_0}{\Delta z} \quad (24\text{c})$$

687 with $\Delta z = z_1 - z_0$ and $\Delta v = v_1 - v_0$. Then, the coefficient a_{\log} is estimated as

$$a_{\log} = v_0 - z_0 d_0 \log z_0 - \frac{\Delta v - z_0 d_0 \log z_1 / z_0}{\Delta z} [z_0 - z_0 \log z_0]. \quad (24\text{d})$$

688 We note that $\log(z_1/z_0)/(z_1 - z_0) \rightarrow 0$ for large z_1 , and as $z_1 = 0.3\delta^+$, this implies that the
 689 second term in c_{\log} only plays a role at low and intermediate Re. Then, a_{\log} can be estimated
 690 as

$$a_{\log} \simeq v_0 - z_0 \left[d_0 \log z_0 - \frac{\Delta v}{\Delta z} (1 - \log z_0) \right] \quad (24\text{e})$$

691 for large Re.

692 **Acknowledgements** Simulations were carried out on the German supercomputing systems
 693 **hawk** at Höchstleistungsrechenzentrum Stuttgart (Bundesprojekt 44187) and **juwels** at Gauss
 694 Centre for supercomputing, Forschungszentrum Jülich (Projects **hku24** and **stadit**). We extend
 695 our thanks to Sally Issa for valuable feedback on the manuscript.

696 Declarations

697 **Author contributions** CA conceived the study, acquired funding, performed the simulation,
698 analysed and plotted the data for this work. CA and HW interpreted the data and compiled
699 the manuscript.

700 **Funding** CA is funded by the European Commission's 7th Framework Programme through
701 the ERC 2019 Starting Grant trainABL (ID 851374). HW is funded by the Ministry for Science
702 and Culture of Lower Saxony (project *ZukunftsKonzept Windenergieforschung*). Open Access
703 funding for this publication through the DEAL agreement.

704 **Data availability** The data is available in long-term repositories and indexed by DOIs as
705 cited in the list of references. Further analysis tools and processed data can be made available
706 upon direct request.

707 **Conflict of interest** The Authors declare no competing interest.

708 **Open access** This article is licensed under a Creative Commons Attribution 4.0 International
709 License, which permits use, sharing, adaptation, distribution and reproduction in any medium
710 or format, as long as you give appropriate credit to the original author(s) and the source,
711 provide a link to the Creative Commons licence, and indicate if changes were made. To view
712 a copy of this licence, visit <https://creativecommons.org/licenses/by/4.0/>.

713 References

- 714 Ansorge C (2019) Scale Dependence of Atmosphere–Surface Coupling Through Similarity The-
715 ory. *Boundary-Layer Meteorol* 170(1):1–27, DOI 10.1007/s10546-018-0386-y
716 Ansorge C (2024a) Direct numerical simulation of turbulent Ekman flow (Re=0500): DOI
717 10.17169/refubium-42505. DOI 10.17169/refubium-42505
718 Ansorge C (2024b) Direct numerical simulation of turbulent Ekman flow (Re=1000): DOI
719 10.17169/refubium-42507. DOI 10.17169/refubium-42507
720 Ansorge C (2024c) Direct numerical simulation of turbulent Ekman flow (Re=1300): DOI
721 10.17169/refubium-42508. DOI 10.17169/refubium-42508
722 Ansorge C (2024d) Direct numerical simulation of turbulent Ekman flow (Re=1600); DOI
723 10.17169/refubium-42509. DOI 10.17169/refubium-42509
724 Ansorge C, Mellado JP (2014) Global Intermittency and Collapsing Turbulence in the Strat-
725 ified Planetary Boundary Layer. *Boundary-Layer Meteorol* 153(1):89–116, DOI 10.1007/
726 s10546-014-9941-3
727 Ansorge C, Mellado JP (2016) Analyses of external and global intermittency in the logarithmic
728 layer of Ekman flow. *J Fluid Mech* 805:611–635, DOI 10.1017/jfm.2016.534
729 Baars WJ, Marusic I (2020) Data-driven decomposition of the streamwise turbulence kinetic
730 energy in boundary layers. Part 2. Integrated energy and. *J Fluid Mech* 882:A26, DOI
731 10.1017/jfm.2019.835
732 Barenblatt GI (1993) Scaling laws for fully developed turbulent shear flows. Part 1. Basic
733 hypotheses and analysis. *J Fluid Mech* 248:513–520, DOI 10.1017/S0022112093000874
734 Barenblatt GI, Goldenfeld N (1995) Does fully developed turbulence exist? Reynolds number
735 independence versus asymptotic covariance. *Phys Fluids* 7(12):3078–3082, DOI 10/bw2sqz
736 Blackadar AK, Tennekes H (1968) Asymptotic Similarity in Neutral Barotropic Plane-
737 tary Boundary Layers. *Journal of the Atmospheric Sciences* 25:1015–1020, DOI 10.1175/
738 1520-0469(1968)025<1015:ASINBP>2.0.CO;2
739 Brown AR, Beljaars ACM, Hersbach H, Hollingsworth A, Miller M, Vasiljevic D (2005) Wind
740 turning across the marine atmospheric boundary layer. *Quarterly Journal of the Royal*
741 *Meteorological Society* 131(607):1233–1250, DOI 10/dw2bxz
742 Calaf M, Meneveau C, Meyers J (2010) Large eddy simulation study of fully developed wind-
743 turbine array boundary layers. *Phys Fluids* 22(1):015,110, DOI 10/b7gc6v
744 Coleman GN, Ferziger JH, Spalart PR (1992) Direct Simulation of the Stably Strati-
745 fied Turbulent Ekman Layer. *Journal of Fluid Mechanics* 244:677–712, DOI 10.1017/
746 S0022112092003264

- 747 da Silva CB, Hunt JC, Eames I, Westerweel J (2014) Interfacial Layers Between Regions
748 of Different Turbulence Intensity. *Annu Rev Fluid Mech* 46(1):567–590, DOI 10.1146/
749 annurev-fluid-010313-141357
- 750 Dimotakis PE (2005) TURBULENT MIXING. *Annual Review of Fluid Mechanics* 37(1):329–
751 356, DOI 10.1146/annurev.fluid.36.050802.122015
- 752 Ekman VW (1905) On the influence of the earth's rotation on ocean currents. *Ark Mat Astron
Fys*, Vol 2 (1905), pp 1-53 2:1–53
- 753 Ellison TH (1955) The Ekman spiral. *Q J Roy Met Soc* 81(350):637–638, DOI 10.1002/qj.
754 49708135025
- 755 Emeis S (2018) Wind Energy Meteorology, 2nd edn. *Atmospheric Physics for Wind Power
Generation*, Springer, Heidelberg
- 756 Emeis S, Baumann-Stanzer K, Piringer M, Kallistratova M, Kouznetsov R, Yushkov V (2007)
757 Wind and turbulence in the urban boundary layer analysis from acoustic remote sensing
758 data and fit to analytical relations. *metz* 16(4):393–406, DOI 10.1127/0941-2948/2007/0217
- 759 Esau I (2004) Simulation of Ekman Boundary Layers by Large Eddy Model with Dynamic
760 Mixed Subfilter Closure. *Environmental Fluid Mechanics* 4(3):273–303, DOI 10/b8f3kh
- 761 Etling D (2002) Theoretische Meteorologie, 2nd edn. *Eine Einführung*, Springer-Verlag, Berlin,
762 Heidelberg
- 763 Etling D (2008) Theoretische Meteorologie: eine Einführung, 3rd edn. Springer, Berlin Heidel-
764 berg
- 765 Foken T (2002) Some aspects of the viscous sublayer. *metz* 11(4):267–272, DOI 10.1127/
766 0941-2948/2002/0011-0267
- 767 Foken Th, Kitajgorodskij SA, Kuznecov OA (1978) On the dynamics of the molecular tem-
768 perature boundary layer above the sea. *Boundary-Layer Meteorol* 15(3):289–300, DOI
769 10.1007/BF02652602
- 770 Ghannam K, Bou-Zeid E (2021) Baroclinicity and directional shear explain departures from
771 the logarithmic wind profile. *Quarterly Journal of the Royal Meteorological Society* 147:434–
772 464, DOI 10/gnj6z2
- 773 Gryning SE, Batchvarova E, Brümmer B, Jørgensen H, Larsen S (2007) On the extension of the
774 wind profile over homogeneous terrain beyond the surface boundary layer. *Boundary-Layer
775 Meteorol* 124(2):251–268, DOI 10.1007/s10546-007-9166-9
- 776 Höglström U (1988) Non-dimensional wind and temperature profiles in the atmospheric surface
777 layer: A re-evaluation. *Boundary-Layer Meteorology* 42:55–78, DOI 10.1007/BF00119875
- 778 Höglström U (1996) Review of some basic characteristics of the atmospheric surface layer.
779 *Boundary-Layer Meteorology* 78(3-4):215–246, DOI 10.1007/BF00120937
- 780 Jacobs AF, Van Boxel JH (1988) Changes of the displacement height and roughness length
781 of maize during a growing season. *Agricultural Forest Meteorol* 42(1):53–62, DOI 10.1016/
782 0168-1923(88)90066-4
- 783 Jiang Q, Wang S, Sullivan P (2018) Large-Eddy Simulation Study of Log Laws in a Neutral
784 Ekman Boundary Layer. *Journal of the Atmospheric Sciences* 75(6):1873–1889, DOI 10.
785 1175/JAS-D-17-0153.1
- 786 Jiménez J (2012) Cascades in Wall-Bounded Turbulence. *Ann Rev Fluid Mech* 44(Volume 44,
787 2012):27–45, DOI 10.1146/annurev-fluid-120710-101039
- 788 Kelly M, Gryning SE (2010) Long-Term Mean Wind Profiles Based on Similarity Theory.
789 *Boundary-Layer Meteorol* 136(3):377–390, DOI 10.1007/s10546-010-9509-9
- 790 Kelly M, Troen I (2016) Probabilistic stability and ‘tall’ wind profiles: Theory and method for
791 use in wind resource assessment. *Wind Energy* 19(2):227–241, DOI 10.1002/we.1829
- 792 Klein M, Maier RE, Schmidt H (2021) Stochastic modeling of transient neutral and stably-
793 stratified Ekman boundary layers. *P A M M* 21(1):e202100146, DOI 10.1002/pamm.
794 202100146
- 795 Li Q, Gentine P, Mellado JP, McColl KA (2018) Implications of Nonlocal Transport and
796 Conditionally Averaged Statistics on Monin–Obukhov Similarity Theory and Townsend’s
797 Attached Eddy Hypothesis. *J Atmos Sci* 75(10):3403–3431, DOI 10.1175/JAS-D-17-0301.1
- 798 Lindvall J, Svensson G (2019) Wind turning in the atmospheric boundary layer over land. *Q
799 J Roy Met Soc* 145(724):3074–3088, DOI 10.1002/qj.3605
- 800 Mellado J, Ansorge C (2012) Factorization of the Fourier transform of the pressure-Poisson
801 equation using finite differences in colocated grids. *Z angew Math Mech* 92(5):380–392,
802 DOI 10.1002/zamm.201100078
- 803 Mellado JP, van Heerwaarden CC, Garcia JR (2016) Near-Surface Effects of Free Atmosphere
804 Stratification in Free Convection. *Boundary-Layer Meteorol* 159(1):69–95, DOI 10.1007/
805

- 807 s10546-015-0105-x
808 Mirocha JD, Churchfield MJ, Muñoz-Esparza D, Rai RK, Feng Y, Kosović B, Haupt SE,
809 Brown B, Ennis BL, Draxl C, Sanz Rodrigo J, Shaw WJ, Berg LK, Moriarty PJ, Linn RR,
810 Kotamarthi VR, Balakrishnan R, Cline JW, Robinson MC, Ananthan S (2018) Large-eddy
811 simulation sensitivities to variations of configuration and forcing parameters in canonical
812 boundary-layer flows for wind energy applications. *Wind Energy Science* 3(2):589–613, DOI
813 10/gn3nh4
814 Moin P, Mahesh K (1998) Direct numerical simulation: A tool in turbulence research. *Annual
815 Review of Fluid Mechanics* 30:539–578, DOI 10.1146/annurev.fluid.30.1.539
816 Momen M, Bou-Zeid E (2016) Large-Eddy Simulations and Damped-Oscillator Models of the
817 Unsteady Ekman Boundary Layer*. *Journal of the Atmospheric Sciences* 73(1):25–40, DOI
818 10.1175/JAS-D-15-0038.1
819 Momen M, Bou-Zeid E, Parlange MB, Giometto M (2018) Modulation of Mean Wind and
820 Turbulence in the Atmospheric Boundary Layer by Baroclinicity. *Journal of the Atmospheric
821 Sciences* 75(11):3797–3821, DOI 10/gfmn67
822 Monin AS (1970) The Atmospheric Boundary Layer. *Annual Review of Fluid Mechanics* 2:225–
823 250, DOI 10.1146/annurev.fl.02.010170.001301
824 Monin AS, Yaglom AM (1975) Statistical Fluid Mechanics, Vol. II, Dover Publications on
825 Physics, vol II. Dover Publications, Inc., Mineola
826 Optis M, Monahan A, Bosveld FC (2014) Moving Beyond Monin-Obukhov Similarity The-
827 ory in Modelling Wind-Speed Profiles in the Lower Atmospheric Boundary Layer un-
828 der Stable Stratification. *Boundary-Layer Meteorology* 153(3):497–514, DOI 10.1007/
829 s10546-014-9953-z
830 Rossby CG, Montgomery RB (1935) The layer of frictional influence in wind and ocean cur-
831 rents. *Papers in Physical Oceanography and Meteorology* III(3):1–101
832 Sakagami Y, Haas R, Passos JC (2020) Generalized Non-dimensional Wind and Temperature
833 Gradients in the Surface Layer. *Boundary-Layer Meteorol* 175(3):441–451, DOI 10.1007/
834 s10546-020-00510-3
835 Spalart PR (1989) Theoretical and numerical study of a three-dimensional turbulent boundary
836 layer. *J Fluid Mech* 205(-1):319, DOI 10.1017/S0022112089002053
837 Spalart PR, Coleman GN, Johnstone R (2008) Direct numerical simulation of the Ekman layer:
838 A step in Reynolds number, and cautious support for a log law with a shifted origin. *Phys
839 Fluids* 20(10):101,507, DOI 10.1063/1.3005858
840 Spalart PR, Coleman GN, Johnstone R (2009) Retraction: “Direct numerical simulation of the
841 Ekman layer: A step in Reynolds number, and cautious support for a log law with a shifted
842 origin” [Phys. Fluids 20, 101507 (2008)]. *Phys Fluids* 21(10):109,901, DOI 10.1063/1.3247176
843 Stoll R, Gibbs JA, Salesky ST, Anderson W, Calaf M (2020) Large-Eddy Simulation of the At-
844mospheric Boundary Layer. *Boundary-Layer Meteorol* 177(2-3):541–581, DOI 10/gmbmzw
845 Svensson G, Holtslag AAM (2009) Analysis of Model Results for the Turning of the Wind
846 and Related Momentum Fluxes in the Stable Boundary Layer. *Boundary-Layer Meteorol*
847 132(2):261–277, DOI 10/bwknmt
848 Tennekes H (1973) A Model for the Dynamics of the Inversion Above a Convective Boundary
849 Layer. *Journal of the Atmospheric Sciences*
850 Townsend AA (1976) The Structure of Turbulent Shear Flow, 2nd edn. Cambridge University
851 Press
852 Van Driest ER (1956) On Turbulent Flow Near a Wall. *Journal of the Aeronautical Sciences*
853 23(11):1007–1011, DOI 10.2514/8.3713
854 Zikanov O, Slinn DN, Dhanak MR (2003) Large-eddy simulations of the wind-induced turbu-
855 lent Ekman layer. *J Fluid Mech* 495:343–368, DOI 10/ccbpbw